Processing and Application of Ceramics 16 [1] (2022) 13–21
https://doi.org/10.2298/PAC2201013S

Doping of alumina ceramics by manganese – Thermodynamical and experimental approach

Jiří Svoboda[1], Katarína Drdlíková[2], Daniel Drdlík[2,3], Aleš Kroupa[1], Jan Michalička[2], Karel Maca[2,3,*]

[1]*Institute of Physics of Materials, Academy of Sciences of the Czech Republic, Brno, Czech Republic*
[2]*CEITEC - Central European Institute of Technology, Brno University of Technology, Brno, Czech Republic*
[3]*Department of Ceramics and Polymers, Faculty of Mechanical Engineering, Brno University of Technology, Brno, Czech Republic*

Received 22 November 2021; Received in revised form 16 December 2021; Accepted 29 December 2021

Abstract

The preparation of a transparent ultra-fine-grained doped ceramics requires a homogeneous dopant distribution in a matrix. In the present work, two thermodynamical phenomena allowing the preparation of such ceramics (the dissolution of the dopant and the formation of undesirable secondary phases) were experimentally and theoretically studied. A general thermodynamic-kinetic model was developed for dopant dissolution, which was verified for the experimental conditions used in this work. The model and experiment showed that Mn_3O_4 dopant with overall concentration of 1 at.% and particle size of 50 nm is dissolved and homogenized in a fine-grained alumina matrix within less than one hour at a temperature of 1220 °C. For the purposes of the study of the formation of undesired secondary phase, the phase diagram of the Al_2O_3-Mn_3O_4 system was calculated using the CALPHAD approach. Detailed STEM observations combined with EDX and EELS chemical analyses showed that the data used for the calculation of the phase diagram need some modifications because they overestimate the solubility of Mn in the alumina and underestimate the solubility of Mn in the $MnAl_2O_4$ spinel.

Keywords: *alumina, doping, sintering, electron energy loss spectroscopy (EELS), thermodynamics*

I. Introduction

Pure and doped alumina found its way to numerous technological applications due to its high hardness, deformation resistance, refractoriness, good thermal stability and excellent corrosion resistance [1]. Doping is usually performed to enhance material properties (mechanical, thermal, etc.) [2,3], to attain some new properties (luminescence, increased conductivity, etc.) [4,5] or to facilitate the preparation conditions (e.g. to lower sintering temperature) [6,7]. In the case of alumina, manganese (Mn) addition is known to enhance both densification and grain growth [8–12]. Moreover, photoluminescence of alumina ceramics can be achieved by Mn doping [13,14]. When combined with ultra-fine-grained pore-free microstructure, functional translucent/transparent alumina ceramics can be obtained [15,16].

In our previous work, translucent/transparent Mn-doped alumina was successfully prepared [15]. To allow homogeneous distribution of dopant, a colloidal approach consisting of intimately mixing of fine alumina powders with Mn_3O_4 nanoparticles was chosen. Sintering was performed by pressure-less pre-sintering up to the closed porosity stage [17] followed by hot isostatic pressing (HIP) at a relatively low temperature of 1200 °C for 3 h under a pressure of 200 MPa in argon. The proposed method limits the grain growth whereby retains fine pore-free microstructure. Even at the addition of 1 at.% of Mn, no secondary phase was observed, contradicting the published results [12]. Our explanation for this phenomenon lies in the differences in the preparation of green bodies, especially in a high level of homogeneity of dopant distribution, and in the final ultra-fine-grained microstructure allowing segrega-

* Corresponding author: tel: +420 541143344,
e-mail: *maca@fme.vutbr.cz*

tion of a significant portion of Mn at grain boundaries as it is shown by Drdlikova *et al.* [15].

Generally, the presence of secondary phases in doped ceramics may be advantageous in terms of suppressing grain growth and obtaining better mechanical properties [18–21]. However, in the case of transparent alumina, it can deteriorate the optical properties [15,19,20]. Also, the intensity of photoluminescence is known to decrease in this case referred to as concentration decay [19]. The secondary phases can, in principle, arise in two ways: i) incomplete dissolution of added dopant or ii) by precipitation from the supersaturated matrix. The system of Mn-doped alumina was used to study both these cases in the present work.

During sintering, the Mn_3O_4 nanoparticles spontaneously dissolve and act as the source of Mn atoms, which substitute some Al atoms in the bulk alumina and at the grain boundaries (GBs), where significant segregation may occur. The paper aims to present experimental results dealing with characterisation of dissolution of Mn_3O_4 nanoparticles during sintering and precipitation of Mn-rich secondary phase. The scanning electron microscopy (SEM) and transmission electron microscopy (TEM) equipped with energy dispersive X-ray analysis (EDX) and electron energy loss spectroscopy (EELS) techniques are used to describe microstructure and chemical composition of the doped material in various doping and sintering regimes and to determine the conditions at which the segregation and/or precipitation occur. Moreover, a general thermodynamic-kinetic model for sintering and grain growth combined with the model for dissolution of dopant particles by diffusion and deposition in bulk as well as their segregation at GBs is developed. The model is experimentally verified for dissolution of Mn_3O_4 nanoparticles in ultra-fine-grained alumina matrix at 1220 °C. To study the formation of secondary phases during thermal treatment of Mn-doped alumina ceramics, the phase diagram of the system Al_2O_3-Mn_3O_4 is constructed using the CALPHAD approach and experimentally verified by the detailed TEM, EDX, and EELS analyses of microstructure after long term heat treatment at 1300 °C.

II. Experimental

Alumina samples doped with 1 and 5 at.% of manganese with respect to alumina were prepared using high purity alumina powder (purity of 99.99%, TM-DAR, Taimei Chemicals Co, Japan) with the primary particle size of ~150 nm and Mn_3O_4 nano-powder (purity higher than 99%, GNM – Getnanomaterials, USA) with the primary particle size of ~50 nm. Water suspensions containing 42 vol.% of alumina were stabilised with 2.2 wt.% of Darvan CN (Vanderbilt Minerals, LLC, USA; composed from water (75%) and ammonium polymethacrylate (25%)) with respect to alumina loading. The suspensions were 24 h milled on rollers with zirconia milling balls. Possible contamination of the samples from the milling was not observed during microstructural analyses. After casting into plastic dishes, the samples were allowed to dry at ambient conditions for several days; subsequent final drying was performed at 60 °C for 10 h. The green bodies were discs with a diameter of 30 mm and a thickness of 3 mm. The green density of samples prior to sintering was 60% of theoretical density.

Sintering of the prepared samples was performed at two temperatures (1220 and 1300 °C) and dwell times (1–10 h) always at the heating rate of 20 °C/min up to the maximal temperature and cooling at the same rate.

Microstructure of the sintered bodies was observed using a high-resolution SEM Lyra 3 (Tescan, Czech Republic) and TEM Titan Themis 60-300 (Thermo Fisher Scientific, USA) equipped with bright-field (BF) and high-angle annular dark field (HAADF) detectors for scanning TEM (STEM) imaging, with energy dispersive X-ray analysis super-X spectrometer (Thermo Fisher Scientific, USA) for EDX and with Quantum ERS/966 post-column energy filter (Gatan, USA) for EELS. Both EDX and EELS analyses were always performed through the acquisition of spectrum images at the identical areas to obtain comparative results of the elemental redistribution. The EDX and EELS data acquisition and quantification were performed by the software Velox v2.14 and GMS3 v3.41, respectively. The mean grain size (MGS) was estimated by the linear intercept method (EN 623-3) using a correction factor of 1.56 [22]. A minimum of 200 grains were measured to obtain a statistically robust set of data.

The Al_2O_3-Mn_3O_4 phase diagram was calculated using the CALPHAD approach by Thermo-Calc software and TCOX5 database.

III. Results and discussion

Three different alumina samples were prepared. Their composition and sintering conditions are summarised in Table 1 together with the selected microstructure features. Microstructures of these samples are shown in Fig. 1.

Table 1. The composition, sintering conditions, and grain size of the individual samples

Sample composition	Sintering conditions	Mean grain size [μm]
Al_2O_3 + 1 at.% Mn	1220 °C/1 h	0.35 ± 0.04
Al_2O_3 + 1 at.% Mn	1300 °C/10 h	2.50 ± 0.40
Al_2O_3 + 5 at.% Mn	1300 °C/10 h	2.50 ± 0.50

The microstructure of all sintered samples was almost fully dense (relative density >99% of theoretical density), with a low number of pores significantly smaller than grains. The sintering at 1220 °C/1 h led to a homogeneous ultra-fine-grained microstructure. The grains grew up to an average value of 2.5 μm after sintering at 1300 °C/10 h for both doping levels. The large values of grain size are a consequence of the heating schedule, and the same value of grain size of both samples

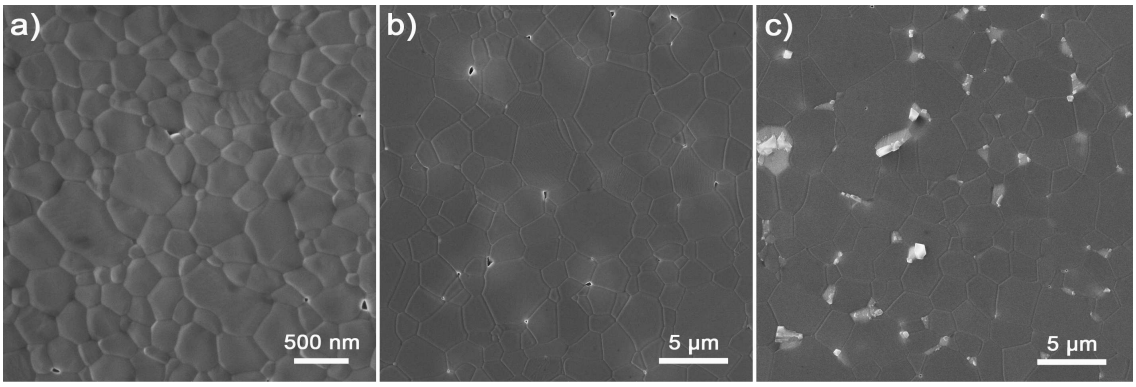

Figure 1. SEM micrographs of: a) 1 at.% of Mn-doped alumina sample sintered at 1220 °C for 1 h and b) 1 at.% and c) 5 at.% of Mn-doped alumina samples sintered at 1300 °C for 10 h

sintered at 1300 °C/10 h is most probably due to the interplay of two phenomena where manganese doping enhances grain growth, while the presence of a secondary phase inhibits grain growth.

As SEM did not reveal any secondary phase in the samples containing 1 at.% of Mn sintered for 1 h at 1220 °C (see Fig. 1a), it is obvious that the Mn_3O_4 dopant was well dissolved and homogenised in alumina even at relatively low temperature during a rather short time. The same situation occurred in the samples with the same Mn content sintered at a higher temperature of 1300 °C and a pronounced dwell time of 10 h, as shown in Fig. 1b.

Application of the last-mentioned sintering procedure (1300 °C/10 h) on the sample with enhanced doping (5 at.% Mn) led to the secondary phase formation documented in Fig. 1c. The secondary phase was dispersed homogeneously across the alumina matrix. The detailed STEM observation of this sample supplemented by EDX analysis shown in Fig. 2 demonstrates the presence of a Mn-rich secondary phase in the form of small grains.

Figure 3a shows elemental mapping at higher magnification, where the segregation of Mn at the alumina/alumina grain boundary occurs. It is evident that a segregation zone enriched by manganese with a thickness of ~3 nm was created along the grain boundary during the thermal treatment. The maximum Mn concentration reached ~1.6 at.% according to EDX analysis (see Fig. 3b and Table 2), and ~2.0 at.% according to EELS analysis (see Fig 3c and Table 2). Moreover, a certain amount of manganese is dissolved in the alumina matrix.

Figure 4a shows the detailed STEM image of the secondary phase/alumina grain boundary and corresponding EDX and EELS line profiles across this boundary.

The chemical compositions of the matrix, alumina/alumina grain boundary area, and inclusion established by EDX and EELS are summarised in Table 2. The concentrations of elements in the matrix and the secondary phase are established by elemental area analysis, and those from grain boundary are taken from line profiles.

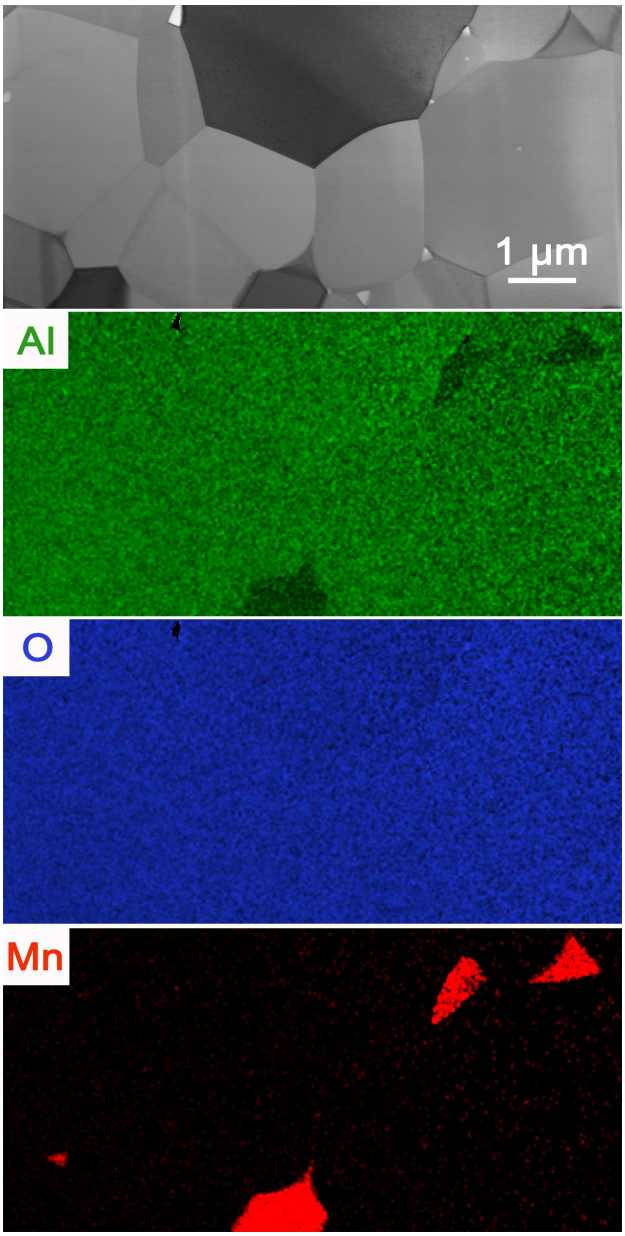

Figure 2. STEM image and corresponding EDX maps of 5 at.% Mn-doped alumina sample sintered at 1300 °C for 10 h

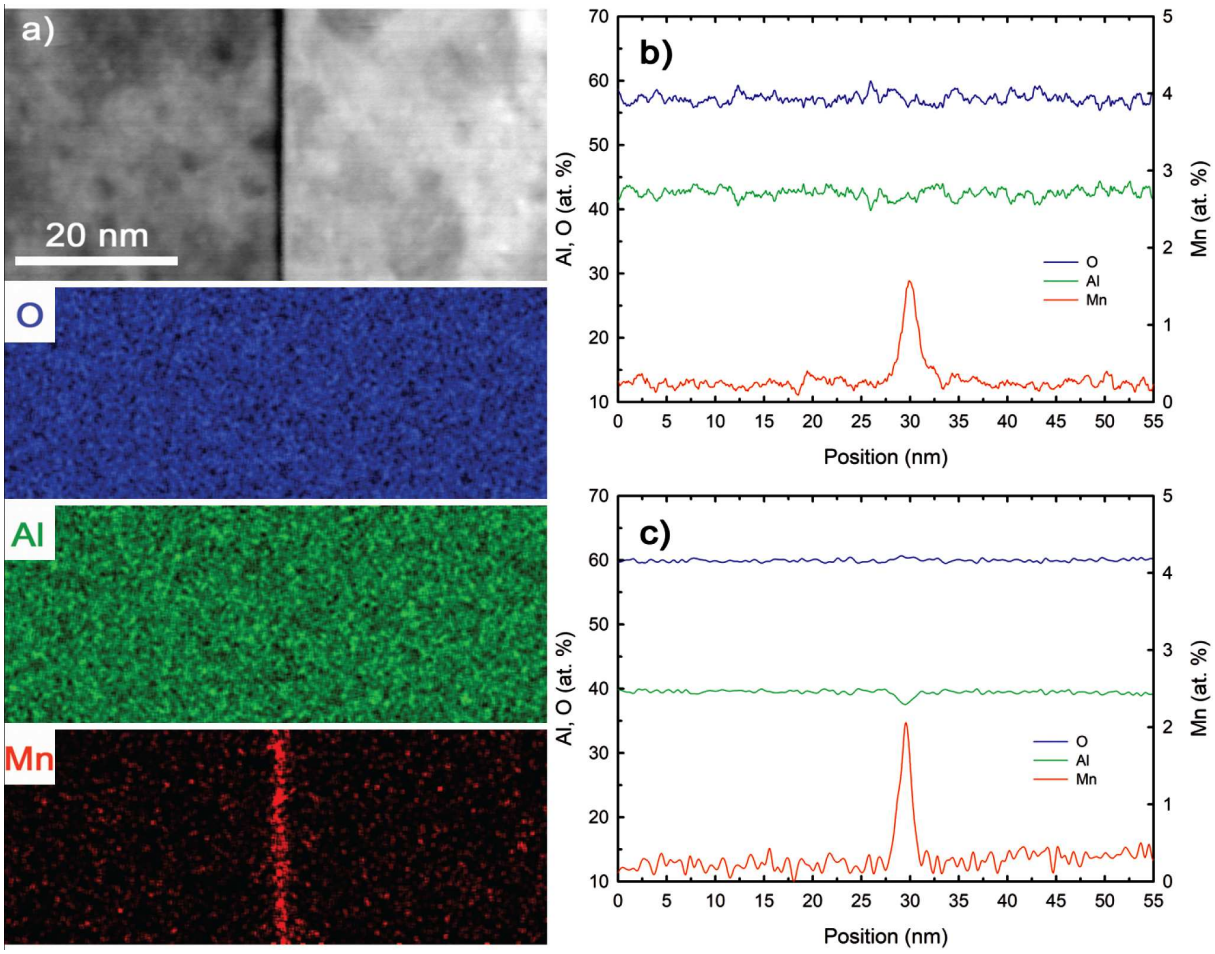

Figure 3. STEM image and EDX maps of 5 at.% of Mn-doped alumina sample sintered at 1300 °C for 10 h (a) showing alumina/alumina grain boundary and corresponding, EDX (b) and EELS (c) line profiles analysis across the grain boundary showing the enhanced concentration of Mn in this location

Table 2. EDX and EELS spectroscopy analysis from different locations in 5 at.% Mn-doped alumina sample

Element	Concentration [at.%]					
	Alumina matrix		Grain boundary		Secondary phase	
	EDX	EELS	EDX	EELS	EDX	EELS
O	58.6	60.0	57.0	60.0	57.3	56.5
Al	43.0	39.7	43.0	38.0	24.2	25.5
Mn	0.2	0.3	1.6	2.0	18.5	18.0

IV. Discussion

4.1. Thermodynamic-kinetic model for dissolution of Mn_3O_4 dopant in alumina during sintering

Our previous results dealing with preparation of Mn-doped translucent/transparent alumina showed that sintering regime consisting of fast pre-sintering and subsequent HIPing for 3 h at 1200 °C is sufficient for dissolving particles of Mn_3O_4 doping powder with mean particle size of 50 nm; neither SEM nor TEM showed any undissolved manganese oxide [15]. In this work, we have broaden our experimental findings that even the pressureless sintering of an alumina powder compact at 1220 °C for only 1 h is sufficient for a complete dissolution of dispersed Mn_3O_4 nanopowder (particle size 50 nm) in alumina compact with initial particle size of 150 nm. To extend the usability of our results to other possible sizes doping powder, a thermodynamic-kinetic model describing the dissolution process is presented in this subsection.

Let us consider one Mn_3O_4 nanoparticle of radius ρ surrounded by a shell of sintering alumina powder of external radius R as a solid unit representing the system, see Fig. 5. The sintering alumina powder has of characteristic grain radius g and porosity p. All mentioned quantities evolve in time.

Assumptions of the model

To treat the problem effectively, let us make the following acceptable assumptions:

- The central Mn_3O_4 nanoparticle dissolves/shrinks with the rate $-\dot{\rho}$, and acts as the source of Mn atoms transported by radial diffusive flux j to the

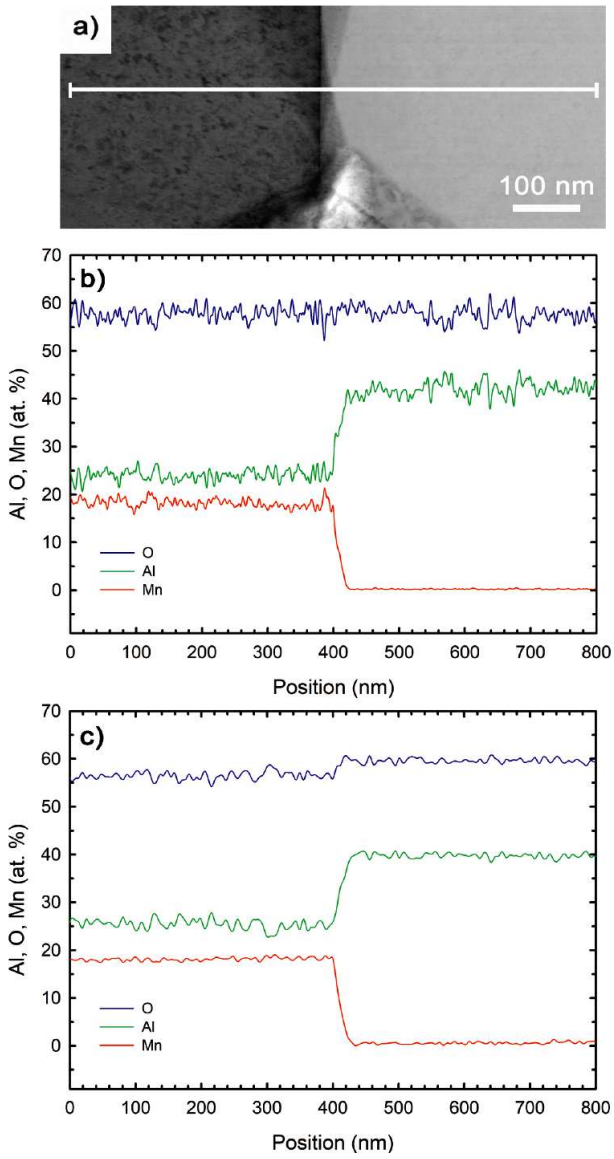

Figure 4. The detailed STEM image (a) of the $MnAl_2O_4$/alumina grain boundary with corresponding EDX (b) and EELS (c) line analysis

alumina shell and deposits both in bulk and at the GBs.

- The solution of Mn and Al atoms in alumina behaves as an ideal solution. Segregation of Mn atoms at GBs is in local equilibrium with the bulk. It is described by trapping energy E corresponding to 1 mol of segregated Mn atoms.
- The model does not treat the diffusion of O and Al atoms as it is assumed to be sufficiently easy, and thus it does not have the influence on the system kinetics nor its control.
- The grain radius g and porosity p evolve according to a respective model for sintering as an independent process. However, the grain radius g and porosity p may influence the effective diffusion coefficient D of Mn atoms in the sintering alumina shell.
- Chemical composition of the shrinking Mn_3O_4 nanoparticle is kept constant, and the site fraction $x_{eq,\rho}$ of Mn atoms at Al positions in alumina at the Mn_3O_4/Al_2O_3 interface is given by the site fraction from the phase diagram x_{eq} and by accounting for the Gibbs-Thomson effect.

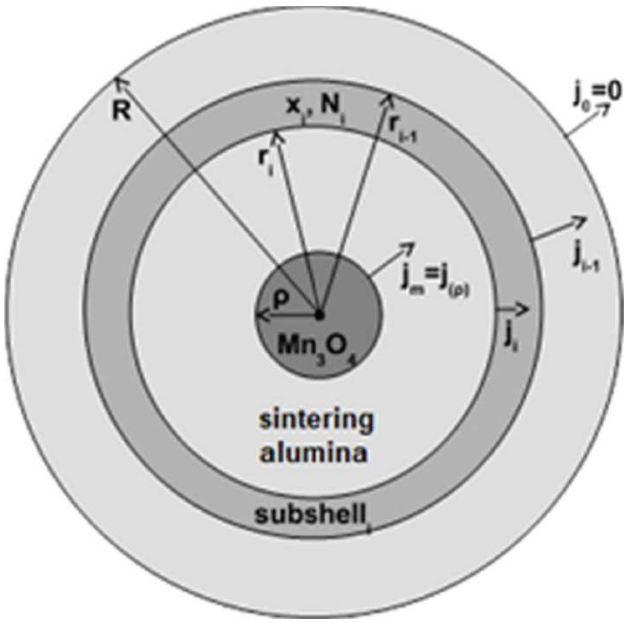

Figure 5. Scheme of the solid unit representing the system

Leading equations of the model

Based on the mass balance for the Mn atoms, the rate of the radius of the Mn_3O_4 nanoparticle $\dot{\rho}$ is linked to the diffusive flux $j(\rho)$ at the Mn_3O_4/Al_2O_3 interface by:

$$\left(\frac{x_{eq,\rho}}{\Omega_{cor}} - \frac{1}{\Omega_{Mn_3O_4}}\right)\dot{\rho} = j(\rho) \tag{1}$$

where Ω_{cor} is the volume corresponding to one mole of Al atoms in alumina and $\Omega_{Mn_3O_4}$ represents the volume of the Mn_3O_4 involving 1 mol of Mn atoms. The Gibbs-Thomson effect is accounted as [23]:

$$x_{eq,\rho} = x_{eq} \exp \frac{2\gamma \cdot \Omega_{Mn_3O_4}}{R_g \cdot T \cdot \rho} \tag{2}$$

The interface specific energy is denoted as γ, R_g is the gas constant and T is the absolute temperature.

The flux in the alumina shell is given by the diffusion equation:

$$\Omega_{cor} j = -D\frac{\partial x}{\partial r} \tag{3}$$

with r being the radial coordinate with the origin in the centre of the Mn_3O_4 nanoparticle and x is the site fraction of Mn atoms at the position r in the alumina shell.

The site fraction of Mn atoms at GBs is given according to the trapping concept as:

$$x_{GB} = x \exp \frac{E}{R_g \cdot T} = K \cdot x \tag{4}$$

To treat the amount of Mn segregated at GBs, the volume fraction of the GBs in the system has to be evaluated. In the case of no porosity, the volume fraction U of the GBs can be calculated as:

$$U = \frac{4\pi \cdot g^2 \cdot \frac{\delta}{2}}{\frac{4}{3}\pi g^3} = \frac{3\delta}{2g} \tag{5a}$$

$$\dot{U} = -\frac{3\delta}{2g^2}\dot{g} \tag{5b}$$

with δ being the thickness of GBs. As the segregation of Mn at the surface can be assumed to be similar to that in GBs, Eq. 4 can also be used for the porous system.

Denoting V_0 as the volume of the system with eliminated pores and V as that with pores, the porosity is defined as:

$$\frac{V - V_0}{V} = p \tag{6}$$

For the given rate $\dot{p}$ the alumina shell shrinks with the strain rate $-\dot{\varepsilon}$ given by:

$$3\dot{\varepsilon} = \frac{\dot{V}}{V} = \frac{\dot{p}}{1-p} \tag{7}$$

To treat the mass conservation in the system, we assume that the alumina shell is divided into m subshells. The subshell i has the inner and outer radii r_i, and r_{i-1}, respectively, while $i = 1, \ldots, m$ with $r_m = \rho$ and $r_0 = R$, see Fig. 5. The subscript i denotes all local quantities in the subshell. The shell shrinks due to the given rate $\dot{p}$ as:

$$\dot{r} = \dot{\varepsilon} \cdot r_i \qquad i = 0, \ldots, m-1 \tag{8}$$

The number of moles N_i of Mn atoms in the subshell i is given by:

$$N_i = \frac{4\pi(r_{i-1}^3 - r_i^3)}{3\Omega_{cor}}(1-p)[1 + U(K-1)]x_i \tag{9}$$

As the number of lattice sites in the subshell i, given by the first two terms in Eq. 8, remains constant during sintering, the rate $\dot{N}_i$, $i = 1, \ldots, m$ is given by applying Eq. 5 as:

$$N_i = \frac{4\pi(r_{i-1}^3 - r_i^3)}{3\Omega_{cor}}(1-p)\left\{\left[1 + \frac{3\delta}{2g}(k-1)\right]\dot{x}_i - (K-1)x_i\frac{3\delta}{2g^2}\dot{g}\right\} \tag{10}$$

The rate $\dot{N}_i$ is given by diffusive fluxes j_i and j_{i-1} at the inner and outer surfaces of the subshell i, see Fig. 5, as:

$$\dot{N}_i = 4\pi\left(j_i \cdot r_i^2 - j_{i-1} \cdot r_{i-1}^2\right) \tag{11}$$

with $j_m = j(\rho)$ and $j_0 = 0$ (condition for the closed system). Putting Eqs. 10 and 11 together, the rate $\dot{x}_i$ is given by:

$$\dot{x}_i = \frac{\frac{3\Omega_{cor}\left(j_i \cdot r_i^2 - j_{i-1} \cdot r_{i-1}^2\right)(1-p)}{r_{i-1}^3 - r_i^3} + (K-1)x_i\frac{3\delta}{2g^2}\dot{g}}{1 + \frac{3\delta}{2g}(K-1)} \tag{12}$$

Using Eq. 2, the diffusive fluxes j_i, $i = 1, \ldots, m$ are given by finite differences as:

$$j_i = \frac{2D}{\Omega_{cor}}\frac{x_{i+1} - x_i}{r_{i-1} - r_{i+1}} \qquad i = 1, \ldots, m-1 \tag{13a}$$

$$j_m = j(\rho) = \frac{2D}{\Omega_{cor}}\frac{x_{eq,\rho} - x_m}{r_{m-1} - \rho} \tag{13b}$$

The rate $\dot{\rho}$ is then given by Eq. 1.

The evolution of porosity during the sintering is treated by detailed models [24,25]. For the demonstration of the present model let us, however, use a simple equation (Eq. 1 in [24]):

$$\dot{\varepsilon} = \frac{\sigma_s}{3K_b} \tag{14}$$

with σ_s being the sintering stress estimated for a rather wide range of conditions from Fig. 8 shown in [3] by:

$$\sigma_s = \frac{\gamma_s}{g} \tag{15}$$

and with K_b being the bulk viscosity estimated from Figs. 1 and 2 shown in [24] as:

$$K_b = 0.05(0.4 - p)\frac{R_g \cdot T \cdot g^3}{\Omega_{cor} \cdot \delta \cdot D_{GB}} \tag{16}$$

The quantity γ_s denotes the specific surface energy and D_{GB} is the grain boundary diffusion coefficient.

The grain growth in porous materials is treated in detail by the model presented in literature [26], where it is shown that the fast surface diffusion can accelerate and the slow one can decelerate the grain growth. For the demonstration of the present model, it is, however, sufficient to assume no influence of porosity on the grain growth and use a simple equation [26]:

$$\dot{g} = \frac{M \cdot \gamma_{GB}}{g} \tag{17}$$

with M being the GB mobility and γ_{GB} the specific GB energy.

Numerical solution and input data

Equations 1–17 provide a complete set of evolution equations for the state variables ρ, R, g and p as well as for the profile of site fraction of Mn $x(r)$ in the alumina shell. For the given starting conditions, the evolution equations can be integrated in time by the Euler method to obtain the system evolution. Equidistant values of r_i are chosen for the initial state. As the Mn_3O_4 nanoparticle shrinks, it is necessary to add the nodal points between ρ and r_{m-1}. This is the case if $r_{m-1} - \rho > 1.5(r_{m-2} - r_{m-1})$. Then the subshell m is divided into two subshells which means that m is increased by 1 and $r_{m-1} = 2r_{m-2} - r_{m-3}$, $r_m = \rho$ and $x_m = x_{m-1}$ are set. If ρ drops below 0.01 of its initial value, the Mn_3O_4 nanoparticle stops acting as the source of Mn atoms, which is ensured by using $r_m = 0$ in Eq.

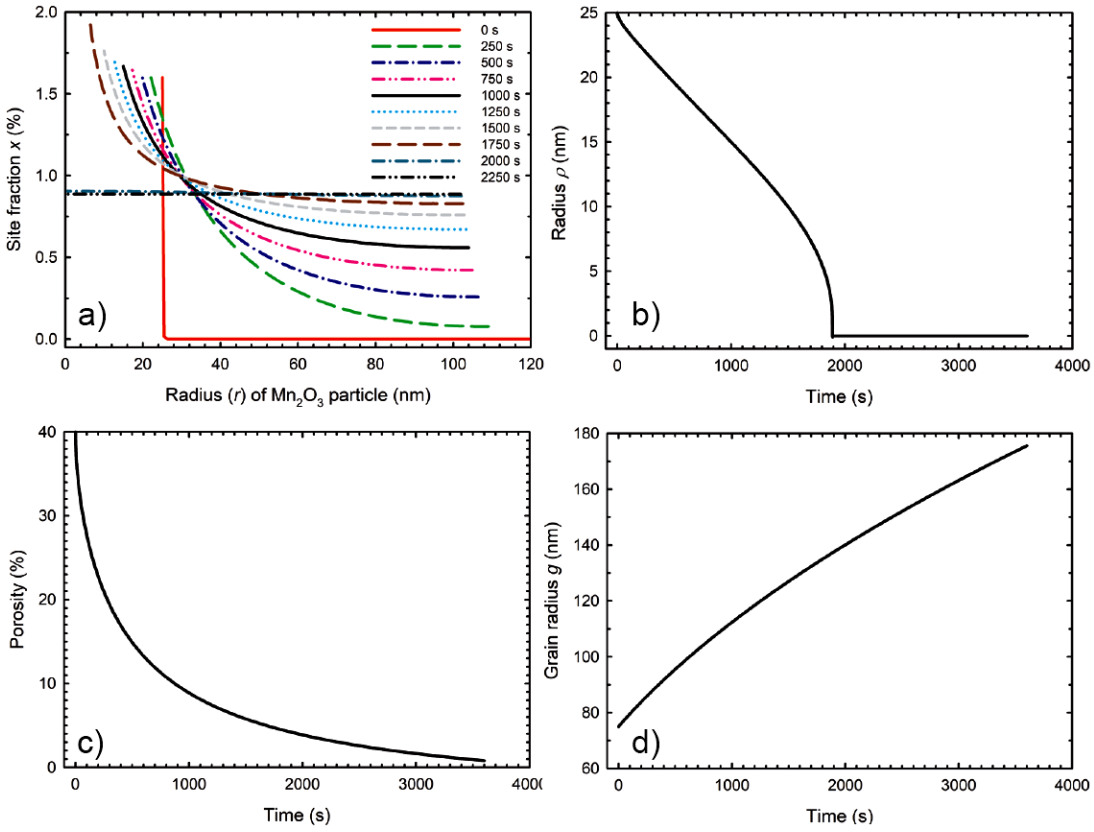

Figure 6. Evolution of: a) the site fraction x profile in sintering alumina shell of Mn atoms stemming from central dissolving Mn_3O_4 nanoparticle, b) the radius of dissolving Mn_3O_4 nanoparticle, c) the porosity of the sintered sample and d) the alumina grain radius in dependence on the sintering time

12 and Eqs. 1 and 2 are not utilized. The calculation is stopped if $x_m - x_1 < 0.01 x_m$ (the $x(r)$ profile becomes sufficiently flat).

The simulation demonstrating the model is performed for the temperature $T = 1220\,°C$ and the following material data are used: $\Omega_{cor} = \Omega_{Mn_3O_4} = 10^{-5}\,m^3/mol$, $x_{eq} = 1\%$, $\delta = 3\,nm$, $\gamma = \gamma_{GB} = \gamma_s = 1\,J/m^2$, $E = 2.1 R_g \cdot T$ (resulting from Eq. 4 using experimental data from EELS analysis), $D = 10^{-17}\,m^2/s$ [27] and enhanced by factor 10 due to much faster GB diffusion, $D_{GB} = 4 \cdot 10^{-16}\,m^2/s$ [28], $M = 5 \cdot 10^{-18}\,m^4/(J{\cdot}s)$ (to fit well the observed grain growth) and initial values of state variables (see Experimental part) $x = 10^{-6}$, $\rho = 25\,nm$, $g = 75\,nm$, $p = 0.40$, $R = 120\,nm$. The results of the simulation are summarised in Fig. 6, where it is shown that the dissolution of the central Mn_3O_4 nanoparticle is completed after about 1900 s (i.e. 32 min) and the equilibration of the x profile is completed after about 2200 s (i.e. 37 min). The kinetics of shrinking of the radius ρ of the Mn_3O_4 nanoparticle can be observed from the motion of the left ends of the x profiles and the kinetics of shrinking of the external radius R of the alumina shell due to sintering can be observed from the motion of the right ends of the x profiles in Fig. 6a).

In this work, the presented model was verified with only one experimental setup ($\rho = 25\,nm$, $g = 75\,nm$, $p = 0.4$, $T = 1220\,°C$, $t = 3600\,s$). In the nearest future our work will focus on broadening the range of experimental conditions ($\rho = 25$–$500\,nm$, $T = 1100$–$1300\,°C$, $t = 100$–$10000\,s$) and further refining the model.

4.2. Formation of the secondary phase in Mn-doped alumina during the heat treatment

After the dissolution of the dopant needed for the functionalization of translucent/transparent alumina ceramics, the formation of the secondary phases, which can be the other source of the unwanted light scattering, must be avoided. Therefore, the second part of the work was dedicated to the study effects of experimental conditions (temperature, time, dopant concentration) on the eventual formation of a second phase (inclusion) in the alumina ceramics.

When the formation of a secondary phase in alumina doped by manganese oxide is to be studied, it is necessary to choose the doping and sintering conditions to provoke the precipitation of secondary phases. This can be achieved by using a higher Mn content and/or higher sintering temperatures and longer sintering time. High temperature and extended dwell time are favourable for grain growth reducing the total grain boundary volume and thus also the amount of Mn ions that can be segregated at grain boundaries.

Our experimental results showed that the heat treatment of the alumina at 1300 °C for 10 h is not enough for the formation of these secondary particles at the

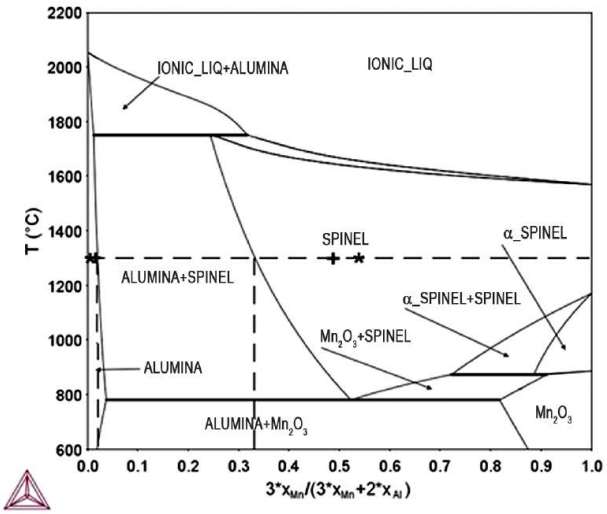

Figure 7. Al_2O_3-Mn_3O_4 phase diagram calculated by CALPHAD approach for the external O_2 pressure of 0.21 bar (SPINEL means $MnAl_2O_4$, α_SPINEL is Mn_3O_4 - the symbols * and + correspond to measurements by EDX analysis and EELS analysis, respectively)

lower level of dopant concentration (1 at.% of Mn, see Fig. 1b), but at the higher dopant concentration (5 at.% of Mn) the Mn-rich inclusions were formed (see Figs. 1c and 2). According to the literature, the secondary phase is alumina-manganese spinel $MnAl_2O_4$ [12,29,30]. $MnAl_2O_4$ particles were dispersed homogeneously across the alumina matrix. The growth of small crystals on the secondary phase during thermal etching was observed, causing a rough surface. Similar surface microstructures were reported by Hernández *et al.* [29] as small pyramids emerged from their "stem grains".

The Al_2O_3-Mn_3O_4 phase diagram shown in Fig. 7 was calculated by the CALPHAD approach for the external O_2 pressure of 0.21 bar corresponding to the normal partial pressure in the air (pure Mn_3O_4 is denoted as α spinel stable at temperatures over 900 °C). The chemical composition on the horizontal axis of the phase diagram is characterised by $3x_{Mn}/(3x_{Mn} + 2x_{Al})$ scale, where x_{Mn} and x_{Al} are molar fractions of Mn and Al, respectively.

EDX and EELS methods are based on two different physical principles and were used complementarily here to eliminate possible experimental error. We can assume that 10 h dwell at temperature of 1300 °C was sufficient for reaching the thermodynamic equilibrium. Therefore, the experimentally determined values of the chemical composition of Mn and Al in the alumina and the spinel determined by both methods can be compared with the equilibrium phase diagram in Fig. 6. The differences among experimental values (measured by EDX and EELS) of solubility of Mn in alumina as well in $MnAl_2O_4$ and that predicted by phase diagram are shown in Table 3.

One can see that the phase diagram slightly overestimates the experimentally determined solubility of Mn in alumina and, on the other hand, the solubility of Mn in spinel is underestimated in the phase diagram compared to experimental values. These experimental findings could contribute to improving the CALPHAD database for the Al_2O_3-Mn_3O_4 system.

Table 3. The comparison of experimental (EDX, EELS) and predicted (from phase diagram) values of solubility of Mn in alumina and $MnAl_2O_4$

	$3x_{Mn}/(3x_{Mn} + 2x_{Al})$* in alumina	$3x_{Mn}/(3x_{Mn} + 2x_{Al})$* in $MnAl_2O_4$
EDX	0.007	0.534
EELS	0.011	0.514
CALPHAD	0.013	0.330

* $3x_{Mn}/(3x_{Mn} + 2x_{Al})$ are the chemical composition characteristics shown in the phase diagram in Fig. 6

Determining the kinetics of precipitation is not the aim of this paper. It can be simulated, e.g. by MATCALC, see work given by Svoboda *et al.* [31] for the respective theory if a reliable CALPHAD database for the Al_2O_3-Mn_3O_4 system is at disposal.

V. Conclusions

Two physico-chemical processes that take place in the preparation of transparent doped ceramic materials, namely the dissolution of dopant precursors in the matrix during an early stage of sintering and the possible formation of undesirable secondary phases at a late stage of sintering, have been studied experimentally and theoretically.

A thermodynamic-kinetic model linking the sintering and dissolution of the dopant precursor provides a prediction of the time required for the homogeneous distribution of the dopant which is controlled by its diffusion across matrix and grain boundaries. The developed model was experimentally validated for the Mn dopant concentration of 1 at.% Mn for the Mn_3O_4 precursor with particle size of 50 nm. It is confirmed that less than one hour at 1220 °C is sufficient to completely dissolve the dopant in an alumina matrix of initial particle size 150 nm and a green density of 60%. Further work will be concentrated on the verification and refinement of the model and will be performed for the dopant precursor sizes up to 500 nm in the range of temperatures 1100–1300 °C and dwell times 100–10000 s.

Experiments have shown that even a 10-hour dwell time at 1300 °C was not sufficient for the formation of a secondary phase at an overall concentration of 1 at.% Mn in the matrix of ultra-fine-grained sintered alumina. The secondary phase of $MnAl_2O_4$ spinel was formed under these conditions when the Mn concentration increased to 5 at.%. The phase diagram of the Al_2O_3-Mn_3O_4 system was constructed using the CALPHAD approach. However, STEM combined with EDX and EELS analysis showed that this phase diagram needs a revision because the CALPHAD approach overestimates the solubility of Mn in alumina and on the other hand underestimates the solubility of Mn in the $MnAl_2O_4$ spinel.

Acknowledgement: This work was funded by the Czech Science Foundation under the grant No. 20-14237S. We also acknowledge CzechNanoLab Research Infrastructure supported by MEYS CR (LM2018110) for allowing the SEM, STEM, EDX, and EELS analysis.

References

1. J. Li, Y. Ye, "Densification and grain growth of Al_2O_3 nanoceramics during pressureless sintering", *J. Am. Ceram. Soc.*, **89** (2006) 139–143.
2. H. Luo, Y. Li, R. Xiang, W. Jia, M. Li, S. Li, D. Lao, H. Wang, Q. Yan, C. Dong, "Exploring the potential of the mechanical/thermal properties and co-shielding ability of Bi_2O_3-doped aluminum borate ceramics against neutron/gamma radiation", *Ceram. Int.*, **47** (2021) 15508–15519.
3. Y. Guo, W. He, H. Guo, "Thermo-physical and mechanical properties of Yb_2O_3 and Sc_2O_3 co-doped $Gd_2Zr_2O_7$ ceramics", *Ceram. Int.*, **46** (2020) 18888–18894.
4. R. Klement, K. Drdlíková, M. Kachlík, D. Drdlík, D. Galusek, K. Maca, "Photoluminescence and optical properties of Eu^{3+}/Eu^{2+}-doped transparent Al_2O_3 ceramics", *J. Eur. Ceram. Soc.*, **41** (2021) 4896–4906.
5. I. Saadeddin, H.S. Hilal, B. Pecquenard, J. Marcus, A. Mansouri, C. Labrugere, M.A. Subramanian, G. Campet, "Simultaneous doping of Zn and Sb in SnO_2 ceramics: Enhancement of electrical conductivity", *Solid State Sci.*, **8** (2006) 7–13.
6. J. Hostaša, F. Picelli, S. Hříbalová, V. Nečina, "Sintering aids, their role and behaviour in the production of transparent ceramics", *Open Ceram.*, **7** (2021) 100137.
7. M.A. Chaika, G. Mancardi, O.M. Vovk, "Influence of CaO and SiO_2 additives on the sintering behavior of Cr,Ca:YAG ceramics prepared by solid-state reaction sintering", *Ceram. Int.*, **46** (2020) 22781–22786.
8. J.R. Keski, I.B. Cutler, "Effect of manganese oxide on sintering of alumina", *J. Am. Ceram. Soc.*, **48** (1965) 653–654.
9. J.R. Keski, I.B. Cutler, "Initial sintering of MnXO-Al_2O_3", *J. Am. Ceram. Soc.*, **51** (1968) 440–444.
10. H. Erkalfa, Z. Misirli, M. Demirci, Ç. Toy, T. Baykara, "The densification and microstructural development of Al_2O_3 with manganese oxide addition", *J. Eur. Ceram. Soc.*, **15** (1995) 165–171.
11. H. Erkalfa, Z. Misirli, T. Baykara, "Densification of alumina at 1250 °C with MnO_2 and TiO_2 additives", *Ceram. Int.*, **21** (1995) 345–348.
12. S.B. Dhuban, S. Ramesh, C.Y. Tan, Y.H. Wong, U. Johnson Alengaram, S. Ramesh, W.D. Teng, F. Tarlochan, U. Sutharsini, "Sintering behaviour and properties of manganese-doped alumina", *Ceram. Int.*, **45** (2019) 7049–7054.
13. I.V. Gasenkova, N.I. Mukhurov, S.P. Zhvavyi, E.E. Kolesnik, A.P. Stupak, "Photoluminescent properties of nanoporous anodic alumina doped with manganese ions", *J. Luminescence*, **185** (2017) 298–305.
14. S.V. Zvonarev, E.I. Frolov, K.Y. Chesnokov, N.O. Smirnov, V.A. Pankov, V.Y. Churkin, "Luminescent properties of alumina ceramics doped with manganese and magnesium", *Optical Mater.*, **91** (2019) 349–354.
15. K. Drdlikova, D. Drdlik, H. Hadraba, R. Klement, K. Maca, "Optical and mechanical properties of Mn-doped transparent alumina and their comparison with selected rare earth and transient metal doped aluminas", *J. Eur. Ceram. Soc.*, **40** (2020) 4894–4900.
16. M. Nagashima, K. Motoike, M. Hayakawa, "Fabrication and optical characterization of high-density Al_2O_3 doped with slight MnO dopant", *J. Ceram. Soc. Jpn.*, **116** (2008) 645–648.
17. T. Spusta, J. Svoboda, K. Maca, "Study of pore closure during pressure-less sintering of advanced oxide ceramics", *Acta Mater.*, **115** (2016) 347–353.
18. E. Brzozowski, M.S. Castro, C.R. Foschini, B. Stojanovic, "Secondary phases in Nb-doped $BaTiO_3$ ceramics", *Ceram. Int.*, **28** (2002) 773–777.
19. K. Drdlikova, R. Klement, H. Hadraba, D. Drdlik, D. Galusek, K. Maca, "Luminescent Eu^{3+}-doped transparent alumina ceramics with high hardness", *J. Eur. Ceram. Soc.*, **37** (2017) 4271–4277.
20. D. Drdlik, K. Drdlikova, H. Hadraba, K. Maca, "Optical, mechanical and fractographic response of transparent alumina ceramics on erbium doping", *J. Eur. Ceram. Soc.*, **37** (2017) 4265–4270.
21. J. Han, P.Q. Mantas, A.M.R. Senos, "Densification and grain growth of Al-doped ZnO", *J. Mater. Res.*, **16** (2011) 459–468.
22. M.I. Mendelson, "Average grain size in polycrystalline ceramics", *J. Am. Ceram. Soc.*, **52** (1969) 443–446.
23. M. Perez, "Gibbs-Thomson effects in phase transformations", *Scripta Mater.*, **52** (2005) 709–712.
24. H. Riedel, H. Zipse, J. Svoboda, "Equilibrium pore surfaces, sintering stresses and constitutive equations for the intermediate and late stages of sintering - II. Diffusional densification and creep", *Acta Metal. Mater.*, **42** (1994) 445–452.
25. J. Svoboda, H. Riedel, H. Zipse, "Equilibrium pore surfaces, sintering stresses and constitutive equations for the intermediate and late stages of sintering - I. Computation of equilibrium surfaces", *Acta Metal. Mater.*, **42** (1994) 435–443.
26. H. Riedel, J. Svoboda, "A theoretical study of grain growth in porous solids during sintering", *Acta Metal. Mater.*, **41** (1993) 1929–1936.
27. B. Lesage, "Some aspects of diffusion in ceramics", *J. Physique III*, **4** (1994) 1833–1850.
28. Y. Tamura, E. Zapata-Solvas, B.M. Moshtaghioun, D. Gómez-García, A. Domínguez-Rodríguez, "Grain-boundary diffusion coefficient in α-Al_2O_3 from spark plasma sintering tests: Evidence of collective motion of charge disconnections", *Ceram. Int.*, **44** (2018) 19044–19048.
29. T. Hernández, C. Bautista, P. Martín, "Synthesis and thermal evolution of Mn-doped alumina nanoparticles by homogeneous precipitation with urea", *Mater. Chem. Phys.*, **92** (2005) 366–372.
30. J.-H. Kim, S.-W. Baik, "Sintering and the optical properties of Mn_3O_4-added Al_2O_3", *J. Korean Inst. Electric. Electron. Mater. Eng.*, **29** (2016) 539–545
31. J. Svoboda, F.D. Fischer, P. Fratzl, E. Kozeschnik, "Modelling of kinetics in multi-component multi-phase multi-particle systems I. Theory", *Mater. Sci. Eng. A*, **385** (2004) 166–174.